Crustal accretion at a sedimented spreading center in the Andaman Sea

Aurélie Jourdain[1], Satish C. Singh[1], Javier Escartin[1], Yann Klinger[1], K.A. Kamesh Raju[2], and J. McArdle[3]
[1]Institut de Physique du Globe de Paris, Sorbonne Paris Cité, UMR7154-CNRS, 1 rue Jussieu, 78238 Paris Cedex 05, France
[2]Council of Scientific and Industrial Research–National Institute of Oceanography, Dona Paula, Goa 403 004, India
[3]Petroleum Geo-Services, 111 Somerset Road, Singapore 238164

ABSTRACT

The magmatic, tectonic, and hydrothermal processes forming the oceanic crust along mid-ocean spreading centers are strongly modified at sedimented spreading centers but poorly understood owing to the lack of good crustal images. Here we present high-resolution deep seismic reflection images across the sedimented slow-spreading Andaman Sea spreading center. Several sub-horizontal sills are injected within the sedimentary strata, and no surface eruption is observed. On-axis reversed-phase reflections within the igneous crust correspond to axial magma lenses at different depths. The faults within the axial valley are steeply dipping (65°–75°) in a staircase pattern forming the axial graben. Their base coincides with a shallow-dipping (30°) reflection, defining the zone of extension and magmatism. As the sill-sediment sequences are rafted away from the axis, they are rotated and buried due to subsidence and faulting, forming the upper oceanic crust. The gabbroic lower oceanic crust is separated from the mantle by a complex Moho transition zone probably containing dunite lenses.

INTRODUCTION

The oceanic crust is formed at mid-ocean spreading centers by a combination of magmatic, tectonic, and hydrothermal processes. In the mid-ocean environment, the oceanic crust consists of extrusive pillow lavas, intrusive dikes, and a thick layer of lower crustal gabbro (Singh and Nicolas, 2015). However, in the vicinity of continents or during the early stages of continental rifting, sediments can bury spreading centers (Einsele, 1985; Lizarralde et al., 2011; Kluesner et al., 2014; Davis and Becker, 2002), significantly modifying the axial thermal regime and fluid circulation, and hence impacting accretion processes (melt emplacement, faulting) and changing the overall lithospheric structure and composition. Here, we present the first whole-crustal, high-resolution multichannel seismic reflection images across the sedimented Andaman Sea spreading center (ASSC), allowing us to determine the interaction between the sedimentation and the magmatic and tectonic processes, and to propose a general model of crustal formation at sedimented mid-ocean ridges.

The back-arc ASSC separates the Burmese sliver plate to the northwest from the Sunda plate (Eurasia) to the southwest (Fig. 1A) (Curray et al., 1979). It connects with the Sagaing strike-slip fault in the north and with the Andaman-Nicobar and Sumatra faults in the south (Singh et al., 2013; Sieh and Natawidjaja, 2000) which result from strain partitioning due to the oblique Indian plate subduction beneath the Sunda plate (Fitch, 1972). Magnetic anomalies indicate that the spreading initiated at 4 Ma at a full rate of 16 mm/yr, increasing to 38 mm/yr at 2 Ma (Kamesh Raju et al., 2004).

Most of the Andaman Sea basin is sedimented and flat, lying at 3000 m water depth. The ASSC, at the center of the basin, displays an ~12-km-wide valley, and a flat-lying valley floor at 3600 m water depth (Fig. 1B), infilled by sediments from the Irrawaddy River system in Myanmar (Curray et al., 1979). This axial graben is bounded by normal faults and tilted fault blocks, a structure reminiscent of that of slow-spreading ridges (Needham and Francheteau, 1974).

SEISMIC DATA

Seismic reflection data were acquired by Petroleum Geo-Services (PGS) in 2008 with a 6400 in^3 air gun array recorded by an 8-km-long streamer with a group spacing of 12.5 m. The air gun and streamer were towed at 8 m and 10 m below the sea surface, respectively, with a 25 m shot interval and a 9 s record length. Data were processed by PGS using a conventional time-migration technique. Stacked data were migrated by PGS using a post-stack Kirchhoff technique. PGS provided the final migrated data and root mean square (RMS) velocities every 1 km (160
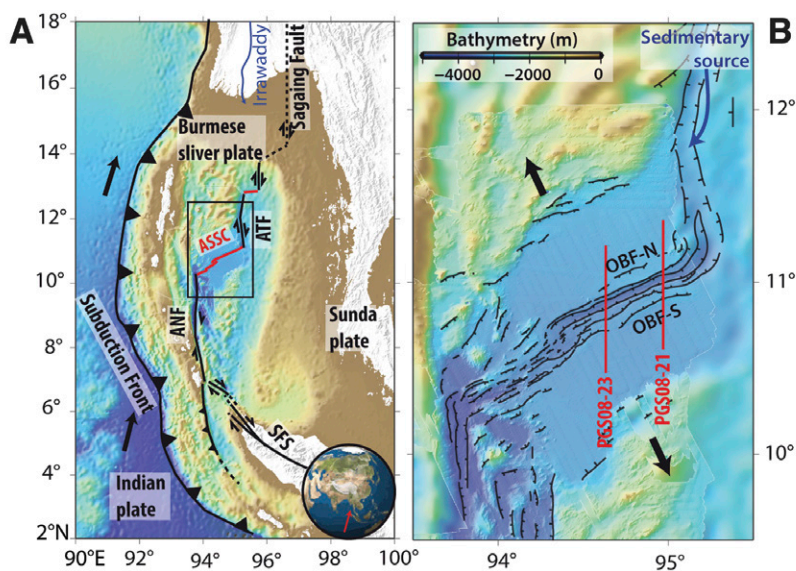
Figure 1. Andaman Sea spreading center. A: General map of study area (multibeam bathymetry from Kamesh Raju et al. [2004] added to the bathymetry of Smith and Sandwell [1997]). Red line shows Andaman Sea spreading center (ASSC). ANF—Andaman-Nicobar fault; SFS—Sumatra fault system; ATF—Andaman transform fault. Black box indicates area shown in B. Arrows indicate sense of movement. B: Detailed map of ASSC. Black lines indicate normal faults. Red lines indicate seismic lines shown in this study. OBF-N—outer bounding fault north; OBF-S—outer bounding fault south.
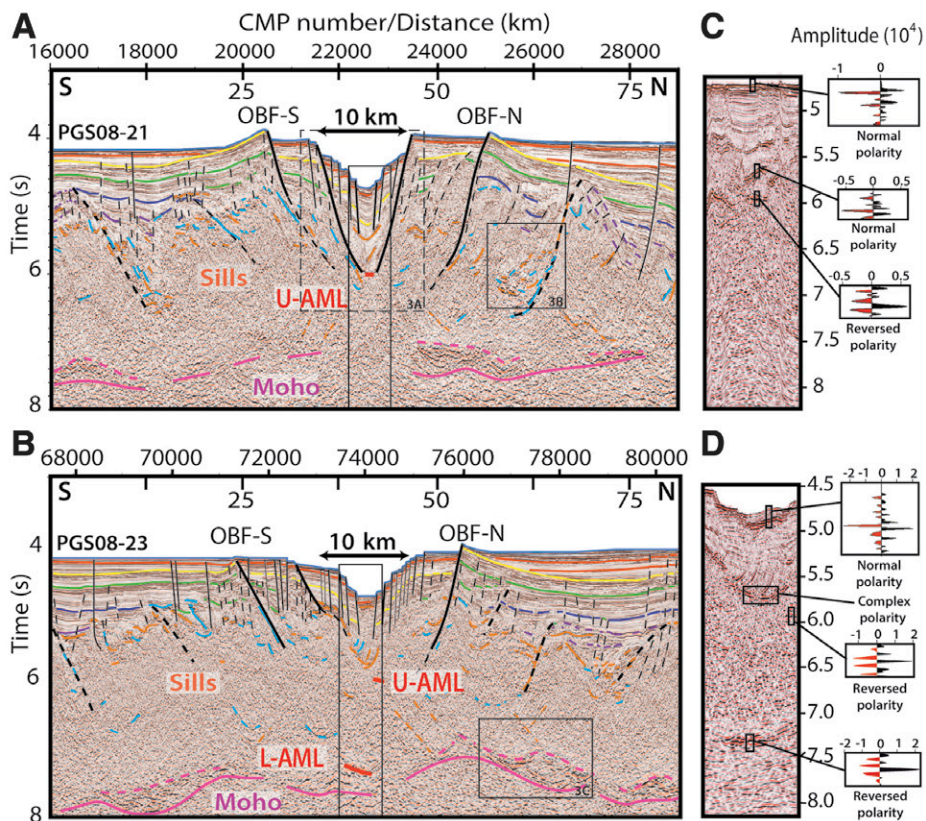
Figure 2. Interpreted seismic images. A: Profile PGS08-21. B: Profile PGS08-23. See Figure 1B for profile locations. Time is two-way traveltime. Black dashed box refers to Figure 3A; other labeled black boxes mark images shown in Figures 3B and 3C. CMP—common mid-point. Blue horizons at top of images indicate seafloor. Active faults are indicated by solid black lines, and inactive by dashed black lines (OBF-N—Outer Bounding Fault North; OBF-S—Outer Bounding Fault South.). Thickness of lines is proportional to offset they induce. High-amplitude normal-phase reflections are highlighted by orange lines, high-amplitude reversed-phase reflections by light blue lines, and Moho by pink lines. Dashed pink lines indicate top of reflective zone above Moho. Thin purple upward through dark orange lines highlight some sedimentary units. Red thick lines mark melt lenses (U-AML—upper axial melt lens; L-AML—lower axial melt lens). Tall black boxes mark images shown in C and D. C: Seafloor flattened image beneath valley floor for profile PGS08-21. Small black boxes indicate seismic trace plots, from top to bottom: polarity of seafloor, polarity of a sill, and polarity of U-AML. D: Seismic image with L-AML flattened. Small black boxes indicate seismic trace plots, from top to bottom: polarity of a sill, complex reflection of a sill, polarity of U-AML, polarity of L-AML.

common mid-points, CMPs); no pre-stack data were available for our study. Here we present two north-south profiles, spaced at ~40 km, crossing the well-sedimented ASSC (Fig. 1B).

Figure 2 shows interpreted seismic time sections along the two profiles that cross the rift valley (see uninterpreted images in Fig. DR1 in the GSA Data Repository[1].) Although the profiles are north-south, 25° off the orthogonal to the spreading axis, symmetry of structures on either side of the axial graben is clear. Thick sediments fill the axial valley, and numerous faults penetrate down 2–2.5 s. The 7.5-s-deep reflection is the Moho, which appears intermittently along both profiles.

In the absence of seismic refraction studies, we converted RMS velocities into interval velocities, laterally smoothed to obtain a continuous velocity and seismic images. Although the RMS-derived interval velocities are much less accurate than those from refraction data, they provide insight into the upper crustal structure. The P-wave velocity increases from 1.6 km/s near the seafloor to 3.0 km/s at the sedimentary sequence base (Fig. DR2). Further below, velocity increases sharply to 4.5 km/s within a 0.6-s-thick zone associated with a layer displaying numerous bright reflections. Below, due to a lack of seismic reflectors, the seismic velocity is poorly constrained.

SEISMIC RESULTS

The sediments, as much as 1.5 s thick, are sub-horizontal (marked by purple to dark orange lines in Fig. 2) and onlap the oceanic crust underneath progressively. Within the sedimentary

layers and underneath them, we observe two sets of strong and discontinuous normal-polarity reflections (in orange, Figs. 2A and 2B), corresponding to high, positive velocity contrasts. We interpret the sub-horizontal reflections (sloping <20°) as solidified igneous bodies or sills within sediments, following criteria used in other studies (Trude et al., 2003; Lizarralde et al., 2011). The steeper reflections (>20°) may correspond to sills and/or dikes injected along faults. As in the Gulf of California (Mexico), amplitude dimming is observed around the sills and could be due to fluid and/or gas expulsion induced by contact metamorphism (Kluesner et al., 2014; Einsele, 1985).

Reversed-Polarity Reflections

Both profiles display some reflections with phase-reversed polarities (in light blue, Figs. 2A–2D), suggesting negative reflection coefficients induced by fluids or by material with lower impedance than that of the surrounding medium. On axis, we observe two reversed-polarity reflectors similar to those observed by Detrick et al. (1987), Kent et al. (1993), and Canales et al. (2009) on fast-spreading ridges, and by Singh et al. (2006) on slow-spreading ridges. Although we are not able to do further analysis, we suggest that, similarly, they possibly correspond to magma-bearing axial melt lenses (AMLs) (thick red lines in Figs. 2A and 2B). The shallowest one is named the upper AML (U-AML). It is 0.8 km wide and is present on both profiles at 6 s two-way traveltime. The second, deeper one is called the lower AML (L-AML). It is 2 km wide and is present only on profile PGS08-23 at 7.2 s.

We also observe some phase-reversed reflections off axis. Most occur along dipping faults, probably corresponding to sill intrusions within sedimentary surroundings or to fault damage zones. Other reversed reflections lie at the sediment interface with the igneous crust or in ponds (Fig. 3B) and could be due to intermixing of sediments and solidified sills. Although we cannot rule out the possible presence of melt sills off axis, we are more confident about the melt lenses beneath the ridge axis associated with the reversed-polarity reflections (U-AML and L-AML). Interestingly, the magma does not erupt to the seafloor, but gets injected within the sediments or along faults.

Faults

The axial graben is flanked by a series of high-angle (65°–75°) normal faults. They have an ~1 km spacing (Figs. 2A, 2B, and 3A) with a staircase pattern, dipping toward the center of the basin, and are responsible for the local subsidence. These faults are recent, as they cut through the most recent sediments. Off-axis faults are relatively inactive and increasingly buried away from the ridge axis, suggesting a
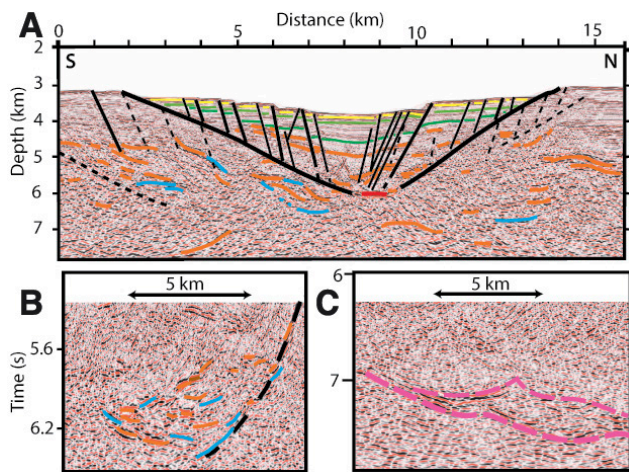
Figure 3. Expanded view of seismic data. Legend is same as in Figure 2 except sediments are delineated at the axis only and with a different color. A: Depth-converted (no vertical exaggeration), seismic image in median valley along profile PGS08-21. Velocity model used is shown in Figure DR2 (see footnote 1). B: Time (not depth converted) section of a buried bounding fault and associated reflections. C: Time (not depth converted) section of a reflective zone above Moho.

syn-tectonic deposition of the sediments with deformation migrating toward the axis.

Further away from the axis and central graben, shallow inward-dipping (20°–40°) reflections are observed on both flanks of the median valley (Figs. 2A, 2B, and 3A). In some cases, these low-angle reflectors reach deep crustal levels and show a clear tilt of the adjacent crust block, suggesting fault-related block rotation resulting in shallow dips of sedimentary reflectors away from the axis. Two prominent ones are named Outer Bounding Fault North and Outer Bounding Fault South (OBF-N and OBF-S in Figs. 2A and 2B). They have an along-axis variable morphology (Fig. 1B) and are more prominent on profile PGS08-21. Another clear, older bounding fault is imaged around CMP 26000–27000 on profile PGS08-21 (Fig. 2A), penetrating down to 700 ms above the Moho, with a 500-ms-thick reflective zone above the fault's lower extent (Fig. 3B). A similar but smaller structure is present on the conjugate side to the south. These low-angle reflections may be akin to the present-day seafloor surface of the axial graben flank. Close to the axis, they rupture the seafloor, whereas off axis, they are sealed by flat-lying onlapping sediments, forming an unconformity. Hence, the faults responsible for the tilt of these blocks are not active anymore. This observation, together with the lack of a tectonic signal on the most recent sediment cover off axis and the concentration of seismicity along the axial graben (Diehl et al., 2013), clearly demonstrate that tectonic deformation concentrates along the graben.

Crust-Mantle Boundary

The Moho reflection is imaged intermittently at ~7.3–7.8 s (Figs. 2A and 2B). It is slightly shallower beneath the axial valley and can be followed along a significant part of the profile. If the base of the sedimentary strata were the top of the oceanic crust and the Moho reflection its base, then crustal thickness would vary from 1.6 s to 2.4 s. On profile PGS08-23, between CMP 77000

and 79000, the Moho displays a complex pattern, with lens-shaped structure (Figs. 2B and 3C); similar reflectors are observed near CMP 16000 and 25000 on profile PGS08-21, and around CMP 69000 and 80000 on profile PGS08-23.

DISCUSSION

A combination of the interval P-wave velocity data and seismic reflection images of the full crustal thickness allows us to characterize for the first time the nature of the whole crust formed along the axis of a sedimented spreading center.

Multiple AMLs have been recently reported beneath fast-spreading centers (Arnulf et al., 2014; Marjanović et al., 2014), but the discovery of two melt sills (U-AML and L-AML) beneath a slow-spreading ridge is novel. The U-AML is relatively shallow when compared to the predicted depth for AMLs for the spreading rate of 3.8 cm/yr (Morgan and Chen, 1993), suggesting that U-AML is likely a transient feature. However, its presence on the two profiles 40 km apart indicates that it is a persistent feature. This

shallow melt lens position could be facilitated by the thick sediment layer blanketing the axial valley, acting as an insulating layer and resulting in a warmer thermal regime that could help retain a melt for a longer time.

The U-AML is at the intersection of the median valley bounding faults, suggesting that there might be some genetic link between these two features, e.g., U-AML acting as a weak zone for the shallow-dipping bounding faults (Ebinger et al., 2010).

The depth of the L-AML, at ~2.3 s below the seafloor or ~4.5 km within the igneous crust, likely feeds the U-AML on axis and may also be the source for other crustal frozen melt sills near and off the spreading axis. Similarly, the L-AML may influence the formation and evolution of the outer bounding faults, separating the brittle crust above from the ductile asthenosphere below it. Similar rheological structure is linked to melt lenses along fast-spreading ridges (e.g., Combier et al., 2008).

Our results show that the crust at the ASSC is formed by a combination of intrusive, metamorphic, and tectonic processes. The basaltic layer 2A, observed at mid-ocean ridges, is replaced by a sill-sediment-metasedimentary layer, explaining the absence of magnetic anomalies on this segment (Kamesh Raju et al., 2004). The steep velocity gradient (3.0–4.5 km/s) is consistent with the numerous reflections observed below the flat sediments (Fig. DR2). It is also consistent with the velocity determined from refraction studies in the Gulf of California (Lizarralde et al., 2007) for sill-sediment layers. The lithology of the high-amplitude reflections below this velocity gradient is difficult to decipher as the velocity is poorly constrained, (Fig. DR2), but based on the presence of strong reflections, we suggest that it might be a continuation of the sill-sediment layer, making the upper crust ~3
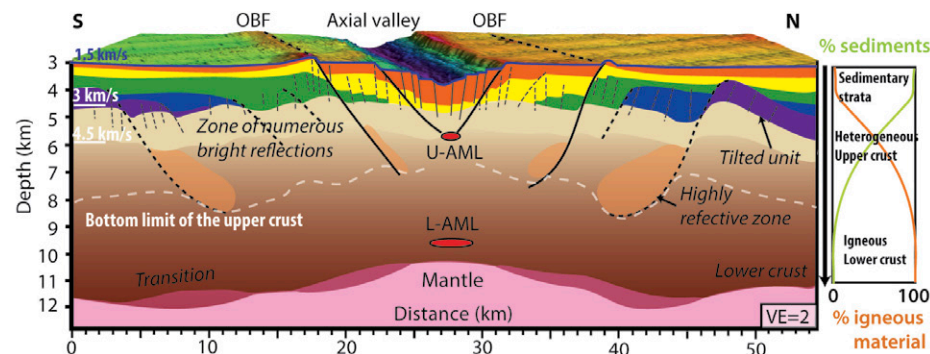
Figure 4. Crustal model of sedimented Andaman Sea spreading center. Schematic three-dimensional block diagram synthesizes different features observed along both profiles. Block diagram differentiates unmetamorphosed sedimentary layers in purple upward to dark orange; mantle transition zone is in dark pink and mantle in light pink. Upper crust with numerous reflections is represented in light brown, lower crust in dark brown. Limit between upper crust and lower crust is probably diffuse and is marked by white dashed line. Marks on left are position of 1.5, 3.0, and 4.5 km/s velocity limits (from Fig. DR2 [see footnote 1]). On right, diagram proposes respective proportions of sediments versus igneous material. OBF—Outer Bounding Fault; U-AML—upper axial melt lens; L-AML—lower axial melt lens; VE—vertical exaggeration.

km thick (Fig. 4). Extension in the rift valley would induce the development of steeply dipping faults (staircase normal faults, Fig. 3A), facilitating further injection of sills, possibly intruding above the older sills and resulting in a thick sill-sediment sequence. After a certain amount of extension and magmatism, a new inner bounding fault would develop inward from the existing bounding faults, the older faults becoming inactive, rafted off axis, and buried by incoming sediments. With such a process, the sill-sediment sequence now present in the graben likely forms the bulk of the upper part of the oceanic crust. We define the base of reflective zone as the sill-sediment upper crust, whose thickness varies across axis, possibly reflecting the interplay between tectonic, sedimentation, and magmatic processes (Einsele, 1985).

Lacking accurate seismic velocities, we assume a P-wave velocity of 6.8 km/s in the lower crust (e.g., Lizarralde et al., 2007). This yields a lower crustal thickness of 3–4.8 km, and thus a total crustal thickness of ~6–7.8 km, overlain by 1.5 km of sediments, consistent with gravity-derived estimations (Morley and Alvey, 2015). The upper crust is somewhat thinner and the lower crust a bit thicker on profile PGS08-23, especially on its southern part. This correlates with a thinner sedimentary layer, suggesting a sediment-supply control on crustal accretion. Off-axis lower crustal melt lenses have been observed at Juan de Fuca Ridge (northwestern North America; Canales et al., 2009) and frozen melt sills below the Moho (Nedimović et al., 2005), but lenses at the ASSC lie within the Moho transition zone, as a possible residue of former L-AMLs. The complex Moho transition zone with dunite-gabbro lenses observed in the Oman ophiolite (Braun and Kelemen, 2002) may be a suitable analog to the complex Moho we image here.

In conclusion, the ASSC corresponds to a particular kind of crustal accretion system. First, there is an absence of an extrusive basalt layer, replaced by a sill-sediment sequence probably consisting of 50% ASSC sediment supply and 50% igneous material emplaced. Second, the magmatic system at the axis shows multiple magma lenses on axis, some of them are maintained at shallow levels of the crust, and the underlying Moho transition is complex and seismically discontinuous. Finally, low-angle rift-bounding faults evolve during accretion, back-tilting the upper crust.

REFERENCES CITED

Arnulf, A.F., Singh, S.C., and Pye, J.W., 2014, Seismic evidence of a complex multi-lens melt reservoir beneath the 9° N overlapping spreading center at the East Pacific Rise: Geophysical Research Letters, v. 41, p. 6109–6115, doi:10.1002/2014GL060859.

Braun, M.G., and Kelemen, P.B., 2002, Dunite distribution in the Oman ophiolite: Implications for melt flux through porous dunite conduits: Geochemistry Geophysics Geosystems, v. 3, 8603, doi:10.1029/2001GC000289.

Canales, J.P., Nedimović, M.R., Kent, G.M., Carbotte, S.M., and Detrick, R.S., 2009, Seismic reflection images of a near-axis melt sill within the lower crust at the Juan de Fuca ridge: Nature, v. 460, p. 89–93, doi:10.1038/nature08095.

Combier, V., Singh, S.C., Cannat, M., and Escartin, J., 2008, Mechanical decoupling and thermal structure at the East Pacific Rise axis 9°N: Constraints from axial magma chamber geometry and seafloor structures: Earth and Planetary Science Letters, v. 272, p. 19–28.

Curray, J.R., Moore, D.G., Lawver, L.A., Emmel, F.J., Raitt, R.W., Henry, M., and Kieckhefer, R., 1979, Tectonics of Andaman Sea and Burma, in Watkins, J.S., et al., eds., Geological and Geophysical Investigations of Continental Margins: American Association of Petroleum Geologists Memoir 29, p. 189–198.

Davis, E.E., and Becker, K., 2002, Observations of natural-state fluid pressures and temperatures in young oceanic crust and inferences regarding hydrothermal circulation: Earth and Planetary Science Letters, v. 204, p. 231–248, doi:10.1016/S0012-821X(02)00982-2.

Detrick, R.S., Buhl, P., Vera, E., Mutter, J., Orcutt, J., Madsen, J., and Brocher, T., 1987, Multi-channel seismic imaging of a crustal magma chamber along the East Pacific Rise: Nature, v. 326, p. 35–41, doi:10.1038/326035a0.

Diehl, T., Waldhauser, F., Cochran, J.R., Kamesh Raju, K.A., Seeber, L., Schaff, D., and Engdahl, E.R., 2013, Back-arc extension in the Andaman Sea: Tectonic and magmatic processes imaged by high-precision teleseismic double-difference earthquake relocation: Journal of Geophysical Research, v. 118, p. 2206–2224, doi:10.1002/jgrb.50192.

Ebinger, C., Ayele, A., Keir, D., Rowland, J., Yirgu, G., Wright, T., Belachew, M., and Hamling, I., 2010, Length and timescales of rift faulting and magma intrusion: The Afar rifting cycle from 2005 to present: Annual Review of Earth and Planetary Sciences, v. 38, p. 439–466, doi:10.1146/annurev-earth-040809-152333.

Einsele, G., 1985, Basaltic sill-sediment complexes in young spreading centers: Genesis and significance: Geology, v. 13, p. 249–252, doi:10.1130/0091-7613(1985)13<249:BSCIYS>2.0.CO;2.

Fitch, T.J., 1972, Plate convergence, transcurrent faults, and internal deformation adjacent to Southeast Asia and the western Pacific: Journal of Geophysical Research, v. 77, p. 4432–4460, doi:10.1029/JB077i023p04432.

Kamesh Raju, K.A., Ramprasad, T., Rao, P.S., Ramalingeswara Rao, B., and Varghese, J., 2004, New insights into the tectonic evolution of the Andaman basin, northeast Indian Ocean: Earth and Planetary Science Letters, v. 221, p. 145–162, doi:10.1016/S0012-821X(04)00075-5.

Kent, G.M., Harding, A.J., and Orcutt, J.A., 1993, Distribution of magma beneath the East Pacific Rise Between the Clipperton Transform and the 9°17′N Deval from forward modeling of common depth point data: Journal of Geophysical Research, v. 98, p. 13,945–13,969, doi:10.1029/93JB00705.

Kluesner, J., Lonsdale, P., and González-Fernández, A., 2014, Late Pleistocene cyclicity of sedimentation and spreading-center structure in the Central Gulf of California: Marine Geology, v. 347, p. 58–68, doi:10.1016/j.margeo.2013.11.001.

Lizarralde, D., et al., 2007, Variation in styles of rifting in the Gulf of California: Nature, v. 448, p. 466–469, doi:10.1038/nature06035.

Lizarralde, D., Adam Soule, S., Seewald, J.S., and Proskurowski, G., 2011, Carbon release by off-axis magmatism in a young sedimented spreading centre: Nature Geoscience, v. 4, p. 50–54, doi:10.1038/ngeo1006.

Marjanović, M., Carbotte, S.M., Carton, H., Nedimović, M.R., Mutter, J.C., and Canales, J.P., 2014, A multi-sill magma plumbing system beneath the axis of the East Pacific Rise: Nature Geoscience, v. 7, p. 825–829, doi:10.1038/ngeo2272.

Morgan, W.J., and Chen, Y., 1993, Dependence of ridge-axis morphology on magma supply and spreading rate: Nature, v. 364, p. 706–708, doi:10.1038/364706a0.

Morley, C.K., and Alvey, A., 2015, Is spreading prolonged, episodic or incipient in the Andaman Sea? Evidence from deepwater sedimentation: Journal of Asian Earth Sciences, v. 98, p. 446–456, doi:10.1016/j.jseaes.2014.11.033.

Nedimović, M.R., Carbotte, S.M., Harding, A.J., Detrick, R.S., Pablo Canales, J., Diebold, J.B., Kent, G.M., Tischer, M., and Babcock, M.J., 2005, Frozen magma lenses below the oceanic crust: Nature, v. 436, p. 1149–1152, doi:10.1038/nature03944.

Needham, H.D., and Francheteau, J., 1974, Some characteristics of the Rift Valley in the Atlantic Ocean near 36°48′ north: Earth and Planetary Science Letters, v. 22, p. 29–43, doi:10.1016/0012-821X(74)90061-2.

Sieh, K., and Natawidjaja, D., 2000, Neotectonics of the Sumatran fault, Indonesia: Journal of Geophysical Research, v. 105, p. 28,295–28,326, doi:10.1029/2000JB900120.

Singh, S.C., and Nicolas, A., 2015, Oceanic spreading center, in Harff, J., et al., eds., Encyclopedia of Marine Geosciences: Dordrecht, Springer Science, doi:10.1007/978-94-007-6644-0124-1.

Singh, S.C., Crawford, W.C., Carton, H., Seher, T., Combier, V., Cannat, M., Canales, J.P., Düsünür, D., Escartin, J., and Miranda, J.M., 2006, Discovery of a magma chamber and faults beneath a Mid-Atlantic Ridge hydrothermal field: Nature, v. 442, p. 1029–1032, doi:10.1038/nature05105.

Singh, S.C., Moeremans, R., McArdle, J., and Johansen, K., 2013, Seismic images of the sliver strike-slip fault and back thrust in the Andaman-Nicobar region: Journal of Geophysical Research, v. 118, p. 5208–5224, doi:10.1002/jgrb.50378.

Smith, W.H.F., and Sandwell, D.T., 1997, Global sea floor topography from satellite altimetry and ship depth sounding: Science, v. 277, p. 1956–1962, doi:10.1126/science.277.5334.1956.

Trude, J., Cartwright, J., Davies, R.J., and Smallwood, J., 2003, New technique for dating igneous sills: Geology, v. 31, p. 813–816, doi:10.1130/G19559.1.